POLITECNICO DI TORINO
Repository ISTITUZIONALE

Microwave sintering of dense and lattice 3Y-TZP samples shaped by digital light processing

(Article begins on next page)

19 April 2024

Microwave sintering of dense and lattice 3Y-TZP samples shaped by Digital Light Processing

Nouhaila Khalile[1], Christophe Meunier[1], Clémence Petit[1]*, François Valdivieso[1], Bartolomeo Coppola[2] and Paola Palmero[2]

[1] Mines Saint-Etienne, Univ Lyon, CNRS, UMR 5307 LGF, F-42023 Saint-Etienne, France

[2] Politecnico di Torino, Department of Applied Science and Technology, INSTM R.U. Lince Laboratory, Corso Duca Degli Abruzzi, 24, Italy

* Corresponding author: Clémence Petit (email: clemence.petit@emse.fr)

Keywords: Zirconia, Digital light processing, Microwave, Densification, Microstructure

Abstract

Nowadays it is possible to produce ceramic parts with solid and complex shapes with rapid and efficient shaping and sintering techniques. In this paper, 3mol% yttria stabilized zirconia (3Y-TZP) dense and lattice parts were shaped by Digital light processing method (DLP) and densified by conventional (CV) and microwave (MW) sintering. 3Y-TZP samples were MW sintered up to 1550 °C with different heating rates (10, 30, and 50 °C/min) for the dense samples and 30 °C/min for the lattice samples. Controlled thermal cycles with a homogenous heating and no thermal runaway was reached. CV sintering was carried out at 10 °C/min up to 1550 °C. No inter-layer delamination was detected after sintering by the two methods. Both dense and lattice MW-sintered samples reached high final densities (equivalent to obtained values with CV-sintered samples, *i.e.*, ≥ 98 % T.D.), but exhibited a lower average grain size than CV-sintered materials. The different architectures between dense and lattice samples resulted in a different specific absorbed power: the power absorbed by the dense sample is lower than that absorbed by the lattice one meaning that this sample architecture heats up easily.

1. Introduction

Technical ceramics are widely used in several applications due to their advantageous properties such as high temperature stability, corrosion resistance, wear resistance and attractive mechanical properties.

Among technical ceramics, yttria-stabilized tetragonal zirconia polycrystal (3Y-TZP) shows outstanding flexural strength and good fracture toughness [1,2], which spreads its application in many different fields (orthopaedic and dental implants, cutting tools, molds, thermal barrier coating, etc). However, an even more extensive use of technical ceramics envisages them to be shaped into complex and customized geometries [3]. Moreover, environmental concerns lead to a need to minimize material, energy and time consumption, especially for the fabrication processes. In the case of ceramics, it applies to all the production steps, particularly shaping and sintering.

To shape green bodies, additive manufacturing (AM) is more and more used for the fabrication of complex structures and to overcome difficulties of conventional shaping techniques. It allows producing layer-by-layer near-net-shape complex shapes from a 3D computer aided design model without expensive tools. For various decades, different AM processes have been developed for ceramic materials [4]. Depending on the form of the starting materials, it exists three categories of AM technologies: bulk solid-based, powder-based and slurry-based methods [5]. Among the slurry-based techniques, robocasting, stereolithography (SLA) and Digital light processing (DLP) have been extensively studied and applied to various ceramics such as alumina, zirconia or calcium phosphates. It is particularly relevant to produce scaffolds for bone tissue engineering which require controlled porosity [6]. DLP is particularly promising because of its high resolution, accuracy and surface finishing [7]. DLP is a type of vat polymerization in which the photopolymerization is performed by a UV projector of a ceramic slurry containing photocurable monomers, a photoinitiator and an appropriate dispersant [8].

The UV projector can cure a complete layer of slurry at once making the process 30-50% shorter that SLA (in which the photopolymerization is performed by a UV laser beam which scans the suspension) while keeping higher quality in the printed parts [9]. In the last few years, several authors aimed at optimizing this process to obtain defect-free and dense samples with high performances. Concerning 3Y-TZP shaping by SLA and DLP, many papers were focused on the optimisation of slurry [10–14], the influence of the printing parameters [15–17] and the optimisation of the debinding and sintering stages [18]. The mechanical properties of the sintered parts were also explored in different researches [15,18–21]. High final densities and mechanical properties were obtained, with values close to those obtained for samples conventionally shaped. For example Chen *et al.* [11] fabricated 3Y-TZP full-ceramic teeth by DLP technology. Lu *et al.* [20] also manufactured 3Y-TZP by DLP technique, providing printed parts with 99% relative density, close to that of conventionally manufactured parts. In a previous study, Coppola *et al.* used DLP to print 3Y-TZP [22] as well as zirconia-toughened alumina samples [21] achieving high relative densities (> 99%), homogeneous and fine microstructures and mechanical properties in line with those of conventionally fabricated materials.

Conventional (CV) sintering of ceramic is generally very slow and energy consuming. Rapid sintering processes as microwave (MW) sintering [23] help to reduce the sintering duration due to the possibility to densify ceramics with high heating rates and low dwell times [24]. Moreover, a fast sintering process allows reaching fine microstructures, which are beneficial for the mechanical properties. Contrary to CV resistive thermal treatment, in the case of MW process, the ceramics heat by direct interaction with the MW, leading to a fast and volumetric heating. The heating capability of a material is linked mainly to its dielectric properties, *i.e.,* the complex permittivity ($\varepsilon^* = \varepsilon' - j\varepsilon''$) and the loss tangent ($\tan(\alpha) = \varepsilon''/\varepsilon'$), where ε' is the dielectric constant and ε'' is the dielectric loss factor. The higher the dielectric loss factor, the

more material couples with the electromagnetic field and heats rapidly. Regarding the dielectric properties, a material can be transparent, absorbent or reflective to MW radiations [25]. For transparent and reflective materials, the so-called hybrid MW heating is performed by the use of a susceptor. The susceptor is a material which strongly couples with MW at low temperature and which is used to initiate the heating and can transmit heat to the sample, mainly via radiation [26]. 3Y-TZP is considered as a transparent material at ambient temperature, but its loss tangent increases sharply with temperature [27]. Thus, direct heating of zirconia by MW is possible but the sharp increase of the loss factor is responsible of temperature runaway (*i.e.,* localized uncontrolled overheating of the sample), which makes very difficult the control of the heating cycle [28]. That is why, in a MW device, an external susceptor is often used to sinter 3Y-TZP [29].

Combining AM shaping and MW sintering appears interesting to overcome the environmental challenges for ceramic production, being this approach still not deeply investigated in literature. The association of robocasting and MW sintering has been tested to produce hydroxyapatite [30] and β-tricalcium phosphate scaffolds [31]. Concerning SLA/DLP and MW sintering, Curto et *al.* [32] sintered by MW alumina lattice structures printed by SLA. In their study, they sintered the samples in a single-mode cavity with a heating rate up to 250 °C/min, reaching relative densities of about 93%. To the best of the authors' knowledge, there is no study involving the use of SLA/DLP joined to MW sintering for 3Y-TZP ceramics.

Therefore, this work is focused on the study of the MW sintering of dense and lattice 3Y-TZP samples made by DLP technique. 3Y-TZP printed parts were sintered in a MW multimode-instrumented device and then characterized in terms of final densities and grain sizes. Identical printed parts were also conventionally sintered for comparison purposes.

2. Materials and methods

2.1. Materials

Samples were prepared using a commercial 3 mol% yttria-tetragonal zirconia polycrystal (3Y-TZP) slurry (Admatec Europe BV, The Netherlands) according to a previous study [21]. In particular, the UV curable slurry contains a photocurable resin with approx. 74.6 wt% ceramic powder loading.

2.2. Shaping of 3Y-TZP parts by DLP

Dense and lattice samples (15 x 4 mm, diameter x height) were designed using the AutoCAD software. Lattice samples have struts with a square section of 0.8 mm side and a porosity of 50%. Parts were printed using a DLP-based additive manufacturing device ADMAFLEX 130 (ADMATEC Europe BV, The Netherlands), in which the ceramic slurry is spread on a plastic foil thanks to a doctor blade and then photopolymerized using a UV projector operating at 405 nm. The printing parameters were fixed as following: 30 μm, 400 ‰ (corresponding to 26.23 mW/cm^2) and 1500 ms, for the layer thickness, LED power and exposure time, respectively. After printing, samples were immersed in deionized water at approx. 40 °C for 24 h to remove extra-slurry. Then, the samples were oven dried at 70 °C for 6 hours, and submitted to thermal debinding up to 1000 °C in an electric furnace (Carbolite 1200, Carbolite Gero GmbH) under air atmosphere as already reported in Figure 1a. The resulting microstructure after thermal debinding is reported in Figure 1b and a homogeneous and constant layer of approx. 29 μm is clearly visible that is in good agreement with the imposed nominal layer of 30 μm.

2.3. CV sintering

The samples were conventionally sintered in an electrical furnace (Carbolite 1800, Carbolite Gero GmbH) with the following thermal cycle: heating rate of 10 °C/min, temperature of 1550 °C and dwell time of 30 min. The CV sintered samples will be referred as D-CV10 and L-CV10, for the dense and lattice samples, respectively.

2.4. MW sintering

MW sintering was carried out in an instrumented multimode MW cavity, already described in details in a previous paper [33]. A schematic view of the setup is shown in Figure 2. This heating cavity of dimensions of 430 mm × 430 mm × 490 mm is connected with a magnetron powered by a 3 kW generator working at a fixed frequency of 2.45 GHz (GMP30K, SAIREM, France). A mixing paddle is used to homogenize the electromagnetic wave in the cavity and to avoid hot spots.

The green samples were positioned in a sintering cell in order to optimize samples' insulation and guarantee their homogeneous heating. This cell was adapted from a cell previously described [33]. The cell mainly contained plates of thermal insulators made of aluminosilicate fibers (KVS 184-400, RATH®, Germany). The use of a SiC ring as a susceptor in the insulating cell allows for a hybrid and uniform heating through the entire sintering process. A bichromatic infrared pyrometer (Lumasense Technology, Germany) was used for temperature measurement. This pyrometer is sensitive to the wavelength between 2 and 2.5 μm and works in the 250-1800 °C temperature range. It was placed above the cavity at around 40 cm from the sample's surface (see Figure 2). To obtain an accurate value of temperature, it is necessary to know the ratio of apparent emissivity k in the experimental conditions. Therefore, a calibration method based on the melting point of a metallic calibration material as described by Zymełka *et al.* [34] and Khalile *et al.* [33] was used. In this study, palladium (Pd: $T_{melting}$ = 1550 °C) was used as

calibrating material. It was placed on a small hole engraved in the sample surface. When Pd started melting, the emissivity ratio k of the IR pyrometer was recalculated so that the melting point of Pd was equal to the measured temperature. A k value of 0.955 was measured and used for the samples of this study. The thermal cycle was controlled by a specific homemade LabVIEW software. It used a PID controller based on the temperature measured by the pyrometer. The incident power delivered by the generator was continuously adjusted during the sintering cycle in order to match the measured temperature with the set temperature. During sintering, the software recorded the data throughout the process.

3Y-TZP dense samples were sintered at 1550 °C with different dwell times. Based on preliminary results of densities and microstructure (data not reported), an optimal dwell time of 30 min was chosen. The applied thermal cycles are presented in Table 1. Dense samples sintered by MW at 10, 30 and 50 °C/min are named D-MW10, D-MW30 and D-MW50 respectively. Lattice sample was MW-heated with a heating rate of 30 °C/min in order to study the influence of the architecture between dense and lattice samples. In this case, the sample is referred as L-MW30.

2.5. Characterization of the sintered samples

Final densities were measured by Archimedes' method following the standard ISO18754-2020 [35] (temperature of 20 °C during the measurement). Theoretical densities of 6.05 g.cm^{-3} was used to calculate the relative densities.

Samples were cut, polished until mirror surface finishing and thermally etched at 1480 °C during 10 min.

The phase composition was analysed by X-Ray Diffraction (XRD). The analyses were carried out with a PANalytical model XPert Pro MPD X-ray diffractometer, using Cu Kα radiation. Operating parameters were as follows: θ - 2θ range: 10-138 °, step angle: 0.013 ° and counting

time: 29 s/step. The XRD patterns were compared with the PDF files of tetragonal ZrO_2 (01-072-2743) and monoclinic ZrO_2 (01-086-1451).

The microstructures were observed using Scanning Electronic Microscopy (SEM, Zeiss SUPRA55VP, Carl Zeiss Microscopy GmbH, Oberkochen, Germany). The average grain sizes of sintered 3Y-TZP were measured by image analysis using the Image J software near the surface and in the bulk of the dense samples and at different locations on the cut surface of the lattice samples.

3. Results & discussion

3.1. Power evolution during sintering

Figure 3 presents the evolution of temperature, forwarded (P_f) and absorbed (P_{abs}) MW powers during the thermal cycles of D-MW10, D-MW30 and D-MW50. Samples were all successfully heated and the measured temperatures follow perfectly the set temperatures without any observed thermal runaway. The P_f and P_{abs} values increase as the set temperature increases during the heating stage. Important oscillations of the P_f and P_{abs} are visible at the beginning of the thermal cycle and the slope of the curves P_{abs} vs time starts changing (increasing) at around 727, 530 and 390 °C for D-MW10, D-MW30 and D-MW50 respectively with a higher slope in the case of D-MW50. Then, a rapid increase of P_f at about 950 °C is observed for all the samples. This latter evolution can be related to the evolution of imaginary part of dielectric permittivity of 3Y-TZP with temperature. Arai *et al.* measured ε'' between 25°C and 1200°C at 2.19 GHz. They observed an increase of ε'' for 3Y-TZP from 500 to 1200°C [36]. Batt *et al.* observed an increase of ε'' between 300 and 600°C [37]. At 1550 °C, during the dwell temperature, the oscillations of P_f and P_{abs} values decrease with increasing heating rates and P_f

is 100 W lower in the case of D-MW50 in comparison with D-MW10 and D-MW30, for which P_f values are very close (between 800 and 850 W).

Figure 4a compares the evolution of the MW powers and temperatures of D-MW30 and L-MW30 samples with almost the same initial dimensions (diameter and thickness) but different architectures. The variations of P_f and P_{abs} for D-MW30 and L-MW30 are almost similar. The sudden increase of P_f at about 1000 °C is also observed for L-MW30. During the dwell at 1550°C, the power oscillations have a lower amplitude for the L-MW30 samples, in comparison with the D-MW30 one. It can indicate a difference of MW/matter interactions between both samples. This can be linked to the variation of the architecture between solid and lattice samples. Figure 4b shows the variation of the specific absorbed power ($P_{sp,}$ power divided by weight of the sample) as a function of temperature. This figure clearly shows that the power absorbed by the dense sample is lower than that absorbed by the lattice one. Thus, this latter heats up easily, therefore the P_f and P_{abs} values increase and remain stable and with lower amplitude of oscillations during the dwell at 1550 °C.

3.2. Density, microstructure and phase composition of solid and lattice sintered samples

The printed samples were successfully debinded and sintered without delamination, as visible in optical microscopy (Figure 5). The final relative densities of the sintered samples are presented in Table 2. Whatever the type of sintering (CV or MW) and the type of samples (dense or lattice) the samples are almost fully dense (relative density > 98 %), without significant differences between samples.

Figure 6 shows low magnification SEM micrographs of the polished sintered samples. The microstructures within the layers are highly dense and homogeneous, with almost no defects. Some micrometer sized residual pores located at the interlayer spaces are detected in few samples, especially in D-MW10 where spherical pores are systematically located at the

interlayer positions. In D-MW30 interlayer pores are sometimes observed, within limited pores located inside the layers. However, for D-MW50 and both L-CV10 and L-MW30 samples, no residual porosity is observed. Starting from a nominal layer thickness of 30 μm, the measured layer thickness (20.02 – 23.39 μm) after sintering (Figure 6) is in good agreement with the expected shrinkage in the z-axis direction [21]. Moreover, the higher layer thickness measured for D-MW10 is representative of a lower degree of densification and consequently shrinkage, consistently with its slightly lower density (Table 2) compared to D-MW30 and D-MW50. The almost full densification makes printing layers less visible or no more visible in the case of D-MW30 and D-MW50 respectively. In the case of D-MW50, no pores are detectable in this material.

By comparing MW and CV sintering at the same heating rate of 10 °C/min (Figures a and d), we can observe smaller layers due to higher shrinkage in the latter material, consistent with its slightly higher sintered density. Finally, SEM micrographs of the lattice samples shows fully dense microstructures, almost defect free, independently on the sintering methods.

Figure 7 shows high magnification SEM micrographs of the samples, confirming their high density and fine-grained and homogeneous microstructures. In addition, in order to ascertain if the unconventional MW sintering could lead to microstructural differences between bulk and surface of the samples, SEM characterization was carried out on both surface and section areas, and compared to the analysis performed on CV-sintered materials. In conventional sintering, the external surface is heated by radiation and convection, being heat conveyed by conduction from the surface to the core of the sample. This means that the heat could be higher at the surface than at the core, potentially producing a certain microstructural difference. In microwave direct processing (*i.e.*, without susceptor), heat is produced in the bulk of the compact and moves towards the external surfaces by radiation and convection. Here, an inverse

thermal gradient takes place as respect to CV sintering, with a higher temperature in the core than at the surface [29].

Results from image analyses, expressed as average grain size and related standard deviation, are collected in Figure 7. All samples have a large grain distribution between 0.1 and 1.2 µm (Figure 7). The average values are in the range 0.3 – 0.6 µm, confirming the fineness and homogeneity of the microstructures obtained by either sintering methods (Table 3). No significant differences between surface and bulk can be observed, and always within the standard deviation. For CV sintering of small samples and standard heating rates, the gradient between core and surface can be in fact typically neglected. In MW direct sintering (*i.e.*, without susceptor), higher average grain size in the bulk of zirconia samples compared to the surface has been previously reported by Charmond *et al.* [29]. But, in our case, the samples were sintered in a hybrid configuration, *i.e.*, assisted with a SiC susceptor. The SiC ring is necessary to initiate heating of 3Y-TZP at low temperature, especially with multimode cavity. In this case, samples are heated by interaction with MW (especially from 500°C for 3Y-TZP, when the loss tangent increases) and by radiative heating of SiC. Our results indicate homogeneous sintering, and thus microstructural development, due to the hybrid configuration, independently on the heating rate. These results are in good agreement with the ones of Charmond *et al.* [29] who obtained a homogeneous microstructure for zirconia samples sintered in a hybrid configuration with a SiC susceptor.

On the opposite, more remarkable differences in microstructural features and thus average grain sizes are observed within the different MW-sintered samples, which can be ascribed to both densification degree and heating rate. Specifically, D-MW30 is characterized by a larger grain size as compared to the other MW-sintered samples (Table 3). If compared to D-MW10 and D-MW50, the larger final grain size can be ascribed to its higher densification degree (see Table 2). Thus, such quick MW sintering processes (*i.e.*, 30 and 50 °C/min) were optimal to reach

high final density and retain a fine grain size. Moreover, by comparing CV and MW sintering at the same heating rate (10 °C/min), a difference can be clearly stated, as D-MW10 sample showed lower average grain size than D-CV10. This can be related to the difference in sintered densities between both samples (98.1% and 99.1%T.D. for D-MW10 and D-CV10 respectively). This can be linked to the difference in the temperature measurement between CV and MW sintering. The temperature is measured by a pyrometer in MW sintering whereas a thermocouple is used in CV sintering. The pyrometer measures the temperature at the surface of the pellet. Thus, the temperature in the sample's core is probably slightly higher than the value measured by the pyrometer. Moreover, the temperature measured by the pyrometer depends on the emissivity obtained by the calibration process described in part 2.4. These two points can bring errors in the temperature measurement for MW sintering. The real temperatures reached by D-CV10 and D-MW10 are probably slightly different.

The microstructure and the average grain sizes of the L-MW30 sample at different zones are presented in Figure 8. The five average values (from 0.35 to 0.43 µm) are slightly similar and shows the homogeneity of the microstructure after MW sintering which indicates a homogeneous heating of the lattice sample.

The comparison between CV and MW sintering for the lattice samples (Table 3) shows lower grain size for the MW-sintered sample (average value of 0.38 µm for L-MW30 and of 0.59 µm for L-CV10). These two samples have similar relative densities (98.6% and 99%). The slightly finer microstructure of the L-MW30 sample can be related to the reduced duration of the thermal cycle (*e.g.*, 90 minutes for the L-MW30 sample and 179 minutes for the L-CV10 one). Indeed, this reduced thermal cycle (approx. 50%) is the most important benefit of the MW sintering.

The microstructure of the L-MW30 sample can also be compared to the microstructure of the D-MW30 one. Both samples underwent the same thermal cycle under MW but they have a

different architecture. Both have similar high densities (98.6% for the L-MW30 sample and 99% for the D-MW30 one). The L-MW30 part has a slightly lower average grain size in comparison with the D-MW30 part (see Table 2 and Figure 8). Based on these results, it is difficult to conclude about a possible impact of the architecture of the sample on the MW heating. Further studies would be needed to sinter under MW different macroporous lattice structures with larger samples.

Finally, the crystalline phases present in the conventionally and MW-sintered samples were identified using XRD analysis and the resulted diffractograms are reported in Figure 9. As expected, the samples are mainly composed of tetragonal phase with the presence of a small amount of monoclinic phase. The comparison of D-MW10, D-CV10 and L-MW10 patterns shows that MW sintering (of dense and lattice samples) did not change the phase composition, in comparison with CV sintering.

In this work, full density and fine microstructures were achieved after MW sintering for DLP-shaped pellets with shorter thermal treatments, in comparison with CV sintering. Curto *et al.* [32] also compared CV and MW sintering of macroporous alumina parts printed by SLA. They also obtained similar high densities and fine microstructures for CV and MW-sintered samples sintered at 1650°C, with a lower duration for MW sintering.

4. Conclusion

Dense and lattice 3Y-TZP samples were successfully printed with DLP technique and sintered under MW. A comparison between CV and MW sintered samples was conducted. The sintered samples were characterized in terms of final densities and microstructure. All the MW-sintered samples exhibited high densities and fine and homogeneous microstructures especially with the high heating rates of 30 and 50 °C/min. Finer microstructures were observed with MW sintering in comparison with CV sintering for both dense and lattice samples. Further, MW sintering

allows a significant reduction of the duration of thermal cycles: for example, the sintering time up to 1550 °C of D-MW50 was 5 times lower than the time needed for D-CV10 with comparable final properties. This study confirms that coupling MW sintering (higher heating rates and lower dwell times) with shaping by AM is an efficient route for a rapid production of technical ceramics, compared to traditional shaping processes (*e.g.*, pressing or casting of suspension) and CV sintering. The fine microstructure resulting from MW sintering is promising for the achievement of high mechanical properties, as it will be performed in a next study. To reduce even more the total processing time, another possibility would be to carry out a MW debinding of the samples.

The present results show a negligible role of the sample architecture on the MW processing, since dense and lattice parts showed comparable final density and microstructure. However, further studies could imply the MW sintering of DLP printed samples with more complex architectures and in different size, and to combine experimental work with simulation studies of propagation of electromagnetic fields inside a new type of ceramic structures.

Declaration of competing interest

The authors declare that they have no known competing financial interests or personal relationships that could have appeared to influence the work reported in this paper.

References

[1]   J. Chevalier, A. Liens, H. Reveron *et al.* Forty years after the promise of "ceramic steel" ? : Zirconia-based composites with a metal-like mechanical behavior , J. Am. Ceram. Soc. 103 (2020) 1482-1513.

[2]   J. Chevalier, L. Gremillard, A.V. Virkar, D.R. Clarke, The Tetragonal-Monoclinic Transformation in Zirconia: Lessons Learned and Future Trends, J. Am. Ceram. Soc. 92 (2009) 1901–1920. https://doi.org/10.1111/j.1551-2916.2009.03278.x.

[3]   T. Ayode Otitoju, P. Ugochukwu Okoye, G. Chen, Y. Li, M. Onyeka Okoye, S. Li, Advanced ceramic components: Materials, fabrication, and applications, J. Ind. Eng. Chem. 85 (2020) 34–65. https://doi.org/10.1016/j.jiec.2020.02.002.

[4]   Y. Lakhdar, C. Tuck, J. Binner, A. Terry, R. Goodridge, Additive manufacturing of advanced ceramic materials, Prog. Mater. Sci. 116 (2021) 100736. https://doi.org/10.1016/j.pmatsci.2020.100736.

[5]   Z. Chen, Z. Li, J. Li, C. Liu, C. Lao, Y. Fu, C. Liu, Y. Li, P. Wang, Y. He, 3D printing of ceramics: A review, J. Eur. Ceram. Soc. 39 (2019) 661-687. https://doi.org/10.1016/j.jeurceramsoc.2018.11.013

[6]   A.P. Moreno Madrid, S.M. Vrech, M.A. Sanchez, A.P. Rodriguez, Advances in additive manufacturing for bone tissue engineering scaffolds, Mater. Sci. Eng. C. 100 (2019) 631–644. https://doi.org/10.1016/j.msec.2019.03.037.

[7]   M. Schwentenwein, J. Homa, Additive Manufacturing of Dense Alumina Ceramics, Int. J. Appl. Ceram. Technol. 12 (2015) 1–7. https://doi.org/10.1111/ijac.12319.

[8]   T. Chartier, C. Chaput, F. Doreau, M. Loiseau, Stereolithography of structural complex ceramic parts, J. Mater. Sci. 37 (2002) 3141–3147. https://doi.org/10.1023/A:1016102210277.

[9]   Š. Jiří, S. Martin, K. Iaroslav, V. Lukáš, A. Michal, T. Veronika, Ceramic 3d printing: Comparison of SLA and DLP technologies, MM Science Journal (2020) 3905-3911. https://doi.org/10.17973/MMSJ.2020_06_2020006.

[10]   J. Sun, J. Binner, J. Bai, 3D printing of zirconia via digital light processing: optimization of slurry and debinding process, J. Eur. Ceram. Soc. 40 (2020) 5837–5844. https://doi.org/10.1016/j.jeurceramsoc.2020.05.079.

[11]   F. Chen, H. Zhu, J.-M. Wu, S. Chen, L.-J. Cheng, Y.-S. Shi, Y.-C. Mo, C.-H. Li, J. Xiao, Preparation and biological evaluation of ZrO2 all-ceramic teeth by DLP technology, Ceram. Int. 46 (2020) 11268–11274. https://doi.org/10.1016/j.ceramint.2020.01.152.

[12]   K. Zhang, C. Xie, G. Wang, R. He, G. Ding, M. Wang, D. Dai, D. Fang, High solid loading, low viscosity photosensitive Al2O3 slurry for stereolithography based additive manufacturing, Ceram. Int. 45 (2019) 203–208. https://doi.org/10.1016/j.ceramint.2018.09.152.

[13]   M. Borlaf, A. Serra-Capdevila, C. Colominas, T. Graule, Development of UV-curable ZrO2 slurries for additive manufacturing (LCM-DLP) technology, J. Eur. Ceram. Soc. 39 (2019) 3797–3803. https://doi.org/10.1016/j.jeurceramsoc.2019.05.023.

[14]   H. Li, Y. Liu, Y. Liu, Q. Zeng, J. Wang, K. Hu, Z. Lu, J. Liang, Evolution of the microstructure and mechanical properties of stereolithography formed alumina cores sintered in vacuum, J. Eur. Ceram. Soc. 40 (2020) 4825–4836. https://doi.org/10.1016/j.jeurceramsoc.2019.11.047.

[15]   X. Fu, B. Zou, H. Xing, L. Li, Y. Li, X. Wang, Effect of printing strategies on forming accuracy and mechanical properties of ZrO2 parts fabricated by SLA technology, Ceram. Int. 45 (2019) 17630–17637. https://doi.org/10.1016/j.ceramint.2019.05.328.

[16]   W. Harrer, M. Schwentenwein, T. Lube, R. Danzer, Fractography of zirconia-specimens made using additive manufacturing (LCM) technology, J. Eur. Ceram. Soc. 37 (2017) 4331-4338 https://doi.org/10.1016/j.jeurceramsoc.2017.03.018.

[17]   C. Marsico, M. Øilo, J. Kutsch, M. Kauf, D. Arola, Vat polymerization-printed partially stabilized zirconia: Mechanical properties, reliability and structural defects, Addit. Manuf. 36 (2020) 101450. https://doi.org/10.1016/j.addma.2020.101450.

[18]   S.H. Ji, D.S. Kim, M.S. Park, J.S. Yun, Sintering Process Optimization for 3YSZ Ceramic 3D-Printed Objects Manufactured by Stereolithography, Nanomaterials. 11 (2021) 192. https://doi.org/10.3390/nano11010192.

[19]   K.-J. Jang, J.-H. Kang, J.G. Fisher, S.-W. Park, Effect of the volume fraction of zirconia suspensions on the microstructure and physical properties of products produced by additive manufacturing, Dent. Mater. 35 (2019) e97–e106. https://doi.org/10.1016/j.dental.2019.02.001.

[20]   Y. Lu, Z. Mei, J. Zhang, S. Gao, X. Yang, B. Dong, L. Yue, H. Yu, Flexural strength and Weibull analysis of Y-TZP fabricated by stereolithographic additive manufacturing and subtractive manufacturing, J. Eur. Ceram. Soc. 40 (2020) 826–834. https://doi.org/10.1016/j.jeurceramsoc.2019.10.058.

[21] B. Coppola, T. Lacondemine, C. Tardivat, L. Montanaro, P. Palmero, Designing alumina-zirconia composites by DLP-based stereolithography: Microstructural tailoring and mechanical performances, Ceram. Int. 47 (2021) 13457–13468. https://doi.org/10.1016/j.ceramint.2021.01.204.

[22] B. Coppola, J. Schmitt, T. Lacondemine, C. Tardivat, L. Montanaro, P. Palmero, Digital light processing stereolithography of zirconia ceramics: Slurry elaboration and orientation-reliant mechanical properties, J. Eur. Ceram. Soc. 42 (2022) 2974–2982. https://doi.org/10.1016/j.jeurceramsoc.2022.01.024.

[23] M. Oghbaei, O. Mirzaee, Microwave versus conventional sintering: A review of fundamentals, advantages and applications, *J. Alloys Comp.* 494 (2010) 175-189. https://doi.org/10.1016/j.jallcom.2010.01.068

[24] S. Ramesh, N. Zulkifli, C.Y. Tan, Y.H. Wong, F. Tarlochan, S. Ramesh, W.D. Teng, I. Sopyan, L.T. Bang, A.A.D. Sarhan, Comparison between microwave and conventional sintering on the properties and microstructural evolution of tetragonal zirconia, Ceram. Int. 44 (2018) 8922–8927. https://doi.org/10.1016/j.ceramint.2018.02.086.

[25] R.R. Mishra, A.K. Sharma, Microwave–material interaction phenomena: Heating mechanisms, challenges and opportunities in material processing, Compos. Part Appl. Sci. Manuf. 81 (2016) 78–97. https://doi.org/10.1016/j.compositesa.2015.10.035.

[26] M. Bhattacharya, T. Basak, A review on the susceptor assisted microwave processing of materials, Energy. 97 (2016) 306–338. https://doi.org/10.1016/j.energy.2015.11.034.

[27] B. Garcia-Baños, J.M. Catalá-Civera, F.L. Peñaranda-Foix, P. Plaza-González, G. Llorens-Vallés, In Situ Monitoring of Microwave Processing of Materials at High Temperatures through Dielectric Properties Measurement, Materials. 9 (2016) 349. https://doi.org/10.3390/ma9050349.

[28] C. Manière, T. Zahrah, E.A. Olevsky, Fully coupled electromagnetic-thermal-mechanical comparative simulation of direct vs hybrid microwave sintering of 3Y-ZrO2, J. Am. Ceram. Soc. 100 (2017) 2439–2450. https://doi.org/10.1111/jace.14762.

[29] S. Charmond, C.P. Carry, D. Bouvard, Densification and microstructure evolution of Y-Tetragonal Zirconia Polycrystal powder during direct and hybrid microwave sintering in a single-mode cavity, J. Eur. Ceram. Soc. 30 (2010) 1211–1221. https://doi.org/10.1016/j.jeurceramsoc.2009.11.014.

[30] Q. Wu, X. Zhang, B. Wu, W. Huang, Effects of microwave sintering on the properties of porous hydroxyapatite scaffolds, Ceram. Int. 39 (2013) 2389–2395. https://doi.org/10.1016/j.ceramint.2012.08.091.

[31] S. Tarafder, V.K. Balla, N.M. Davies, A. Bandyopadhyay, S. Bose, Microwave-sintered 3D printed tricalcium phosphate scaffolds for bone tissue engineering, J. Tissue Eng. Regen. Med. 7 (2013) 631–641. https://doi.org/10.1002/term.555.

[32] H. Curto, A. Thuault, F. Jean, M. Violier, V. Dupont, J.-C. Hornez, A. Leriche, Coupling additive manufacturing and microwave sintering: A fast processing route of alumina ceramics, J. Eur. Ceram. Soc. 40 (2020) 2548–2554. https://doi.org/10.1016/j.jeurceramsoc.2019.11.009.

[33] N. Khalile, C. Petit, C. Meunier, F. Valdivieso, Hybrid microwave sintering of alumina and 3 mol% Y2O3-stabilized zirconia in a multimode cavity – Influence of the sintering cell, Ceram. Int. (2022). https://doi.org/10.1016/j.ceramint.2022.03.072.

[34] D. Žymełka, S. Saunier, J. Molimard, D. Goeuriot, Contactless Monitoring of Shrinkage and Temperature Distribution during Hybrid Microwave Sintering, Adv. Eng. Mater. 13 (2011) 901–905. https://doi.org/10.1002/adem.201000354.

[35] International Organisation for Standardization, *Fine ceramics (advanced ceramics, advanced technical ceramics) — Determination of density and apparent porosity.* ISO18754:2020, 2020, 10 pages.

[36] M. Arai, J.G.P. Binner, T.E. Cross, Comparison of Techniques for Measuring High-Temperature Microwave Complex Permittivity: Measurements on an Alumina/Zircona System, J. Microw. Power Electromagn. Energy. 31 (1996) 12–18. https://doi.org/10.1080/08327823.1996.11688287.

[37] J. Batt, W.H. Sutton, J.G.P. Binner, T.E. Cross, A parallel measurement programme in high temperature dielectric property measurement: An update, American Ceramic Society (ACS) annual meeting and exposition (1995).

Figures' and tables' captions

Figure 1: (a) Thermal debinding cycle (total duration of the cycle: 58h50) and (b) FE-SEM micrograph of a sample cross section (fracture surface) after thermal debinding

Figure 2: Schematic of the hybrid MW sintering configuration

Figure 3: Thermal cycle and power evolution during MW sintering of dense samples: (a) D-MW10, (b) D-MW30 and (c) D-MW50

Figure 4: Evolution of (a) MW powers and temperatures *vs* time and (b) specific P_{abs} during MW sintering of dense and lattice samples

Figure 5: (a) Pictures of green and sintered L-MW30 sample and (b) Optical microscope image of the surface of this sample

Figure 6: SEM micrographs (bulk) of dense and lattice MW and CV sintered samples

Figure 7: SEM micrographs and grain size distributions of MW and CV sintered 3Y-TZP samples at the surface (red color) and in the bulk (blue color) of the sample

Figure 8: SEM micrographs and average grain size at different zones of the cut surface of L-MW30

Figure 9: XRD diffractograms corresponding to D-CV10, D-MW10 and L-MW30 samples (m = monoclinic ZrO_2 and t = tetragonal ZrO_2)

Table 1: Thermal cycles for MW and CV sintering

Table 2: Relative densities of MW and CV sintered samples

Table 3: Grain sizes (µm) in the surface and the bulk of MW end CV sintered samples (note that the values for L-MW30 are not indicated here and are given in Figure because different measurements were carried out at different locations for this sample)

Table 1

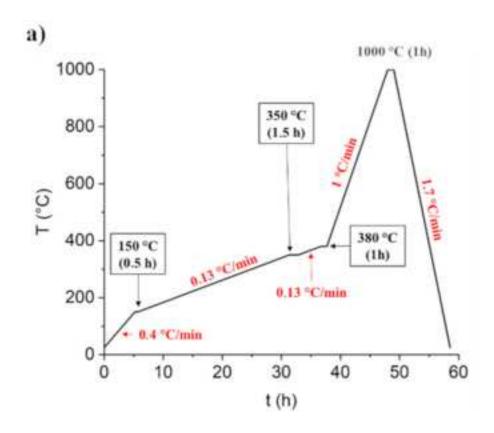| Sample	Sintering process	Heating rate (°C/min)	Dwell time (min)
D-MW10		10	
D-MW30	MW	30	30
D-MW50		50	
D-CV10	CV	10	30
L-MW30	MW	30	30
L-CV10	CV	10	30

Table 2

	D-MW10	D-MW30	D-MW50	D-CV10	L-MW30	L-CV10
Density (%T.D.)	98.1±0.1	99.0±0.2	98.9 ±0.1	99.1±0.2	98.6±0.1	99.0±0.1

Table 3

	D-MW10	D-MW30	D-MW50	L-MW30	D-CV10	L-CV10
Surface	0.38 ± 0.11	0.50 ± 0.14	0.40 ± 0.14		0.55 ± 0.16	0.51 ± 0.15
				Figure 8		
Bulk	0.34 ± 0.10	0.55 ± 0.15	0.43 ± 0.14		0.58 ± 0.15	0.53 ± 0.16

a)

b)

a)

b)

a)   Green   As-sintered

b)   500 μm

a) D-MW10
23,39 μm
23,39 μm
22,30 μm
22,90 μm
20 μm

b) D-MW30
20,15 μm
21,95 μm
21,44 μm
20,20 μm
20 μm

c) D-MW50
20 μm

d) D-CV10
20,01 μm
20,46 μm
21,44 μm
20 μm

e) L-MW30
20 μm

f) L-CV10
20 μm

Zone I

Zone II

Zone III

Zone IV

Zone V

1 μm